

Dynamical detection of mean-field topological phases in an interacting Chern insulator

Wei Jia,^{1,2} Long Zhang,^{3,1,2} Lin Zhang,^{4,1,2} and Xiong-Jun Liu^{1,2,5,6,*}

¹*International Center for Quantum Materials and School of Physics, Peking University, Beijing 100871, China*

²*Collaborative Innovation Center of Quantum Matter, Beijing 100871, China*

³*School of Physics, Huazhong University of Science and Technology, Wuhan 430074, China*

⁴*ICFO-Institut de Ciències Fotoniques, The Barcelona Institute of Science and Technology,
Av. Carl Friedrich Gauss 3, 08860 Castelldefels (Barcelona), Spain*

⁵*CAS Center for Excellence in Topological Quantum Computation,
University of Chinese Academy of Sciences, Beijing 100190, China*

⁶*Institute for Quantum Science and Engineering and Department of Physics,
Southern University of Science and Technology, Shenzhen 518055, China*

Interactions generically have important effects on the topological quantum phases. For a quantum anomalous Hall (QAH) insulator, the presence of interactions can qualitatively change the topological phase diagram which, however, is typically hard to measure in the experiment. Here we propose a novel scheme based on quench dynamics to detect the mean-field topological phase diagram of an interacting Chern insulator, with nontrivial dynamical quantum physics being uncovered. We focus on a two-dimensional QAH system in the presence of a weak to intermediate Hubbard interaction which mainly induces a ferromagnetic order under the mean-field level. After quenching the Zeeman coupling, both the mean-field Hamiltonian and many-body quantum state evolve over time. This is in sharp contrast to quenching a non-interacting system, in which only the many-body state evolves. We find two characteristic times t_s and t_c which capture the emergence of dynamical self-consistent particle number density and dynamical topological phase transition for the time-dependent Hamiltonian, respectively. An interesting result is that $t_s > t_c$ ($t_s < t_c$) occurs in repulsive (attractive) interaction when the system is quenched from an initial fully polarized state to the topologically nontrivial regimes, and $t_s = t_c$ characterizes the topological phase boundaries. Moreover, the topological number of mean-field topological phase is determined by the spin polarizations of four Dirac points at the time t_s . With these results we provide a feasible scheme to detect the mean-field topological phase diagram via the two characteristic times in quench dynamics, which can reveal the novel interacting effects on the topological phases and shall promote the experimental observation.

I. INTRODUCTION

Topological quantum phase is currently a mainstream of research in condensed matter physics [1–5]. At equilibrium, the topological phases can be characterized by nonlocal topological invariants [6, 7] defined in ground states. This classifies the gapped band structures into distinct topological states, with great success having been achieved in study of topological insulators [8–11], topological semimetals [12–15], and topological superconductors [16–20]. In general, a noninteracting topological phase can be greatly affected after considering many-body interaction [21–30]. For instance, the repulsive Hubbard interaction can drive a trivial insulator into a topological Mott insulator [31–33], while the attractive Hubbard interaction may drive a trivial phase of two-dimensional (2D) quantum anomalous Hall (QAH) system into a topological superconductor/superfluid [34–37]. Nevertheless, how to accurately identify the topological phases driven by the interactions is still a fundamental issue and usually hard in experiments.

In recent years, the rapid development of quantum simulations [38–40] provides new realistic platforms to explore exotic interacting physics, such as ultracold

atoms in optical lattices [41–47] and superconducting qubits [48–50]. A number of topological models have been realized in experiments, such as the 1D Su-Schrieffer-Heeger model [51, 52], 1D AIII class topological insulator [53, 54], 1D bosonic symmetry-protected phase [55, 56], 2D Haldane model [57], the spin-orbit coupled QAH model [58–60], and the 3D Weyl semimetal band [61, 62]. Accordingly, the various detection schemes for the exotic topological physics are also developed, ranging from the measurements of equilibrium topological physics [63–66] to non-equilibrium quantum dynamics [67–75]. In particular, the dynamical characterization [76–81] shows the correspondence between broad classes of equilibrium topological phases and the emergent dynamical topology in far-from-equilibrium quantum dynamics induced by quenching such topological systems, which brings about the systematic and high-precision schemes to detect the topological phases based on quantum dynamics and has advanced broad studies in experiment [82–91]. Nevertheless, in the current these studies have been mainly focused on the noninteracting topological systems, while the particle-particle interactions are expected to have crucial effects on the topological phases, whose detection is typically hard to achieve. For example, when quenching an interacting topological system [92–95], both the interactions and many-body states of the system evolve simultaneously after quenching, leading to complex nonlinear quantum dynamics [96–99] and exotic nonequilib-

* Correspondence addressed to: xiongjunliu@pku.edu.cn

rium phenomena [100–103].

In this paper, we propose a novel scheme based on quench dynamics to detect the mean-field topological phase diagram of an interacting Chern insulator, with nontrivial dynamical quantum physics being uncovered. Specifically, we consider a 2D QAH system in presence of a weak to intermediate Hubbard interaction which mainly induces a ferromagnetic order under the mean-field level. The interaction corrects the Zeeman coupling to an effective form and the equilibrium topological properties are fully determined by the self-consistent Zeeman potential. By quenching the system from an initial near fully polarized trivial state to a parameter regime in which the equilibrium phase is topologically nontrivial, we uncover two dynamical phenomena rendering the dynamical signals of the equilibrium mean-field phase. (i) There are two characteristic times t_s and t_c capturing the emergence of dynamical self-consistent particle number density and dynamical topological phase transition for the time-dependent Hamiltonian, respectively, with $t_s > t_c$ ($t_s < t_c$) occurring in the repulsive (attractive) interaction and $t_s = t_c$ on topological phase boundaries. (ii) The topological number of the equilibrium mean-field phase after quench is determined by the spin polarization of four Dirac points at the time t_s in examining spin dynamics. Under the two fundamental properties, we employ the characteristic times to establish a dynamical detection scheme of topological phase in the interacting system. With feasibility of measuring the time scales in dynamical evolution, this scheme provides a simplified way to detect the mean-field phase diagram in an interacting Chern matter and may be applied to the quantum simulation experiments in the near future.

The remaining part of this paper is organized as follows. In Sec. II, we introduce the QAH-Hubbard model. In Sec. III, we study the quench dynamics of the system. In Sec. IV, we reveal the nontrivial dynamical properties in quench dynamics. In Sec. V, we determine the equilibrium mean-field topological phases via the dynamical properties. In Sec. VI, we establish the nonequilibrium detection scheme for the real measurements of mean-field topological phase diagram. Finally, we summarize the main results and provide the brief discussion in Sec. VII.

II. QAH-HUBBARD MODEL

Our starting point is a minimal 2D QAH model [34, 36], which has been recently realized in cold atoms [58, 60, 82, 84], together with an attractive or repulsive on-site Hubbard interaction of strength U . The QAH-Hubbard Hamiltonian reads

$$H = \sum_{\mathbf{k}} C_{\mathbf{k}}^\dagger \mathcal{H}_{\mathbf{k}}^{(0)} C_{\mathbf{k}} + U \sum_{\mathbf{j}} n_{\mathbf{j}\uparrow} n_{\mathbf{j}\downarrow}, \quad (1)$$

$$\mathcal{H}_{\mathbf{k}}^{(0)} = \mathbf{h}_{\mathbf{k}} \cdot \boldsymbol{\sigma} = [m_z - 2t_0(\cos k_x + \cos k_y)] \sigma_z + 2t_{s0} \sin k_y \sigma_x + 2t_{so} \sin k_x \sigma_y,$$

where $C_{\mathbf{k}} = (c_{\mathbf{k}\uparrow}, c_{\mathbf{k}\downarrow})^T$ is the spinor operator of momentum \mathbf{k} , $n_{\mathbf{j}s} = c_{\mathbf{j}s}^\dagger c_{\mathbf{j}s}$ with $s = \uparrow$ or \downarrow is the particle number operator at site \mathbf{j} , $\sigma_{x,y,z}$ are the Pauli matrices, and m_z is the Zeeman coupling. Here t_0 and t_{so} are the spin-conserved and spin-flipped hopping coefficients, respectively. In the noninteracting case, the Bloch Hamiltonian $\mathcal{H}_{\mathbf{k}}^{(0)}$ produces two energy bands $\pm e_{\mathbf{k}} = \pm \sqrt{h_{x,\mathbf{k}}^2 + h_{y,\mathbf{k}}^2 + h_{z,\mathbf{k}}^2}$, for which the gap can be closed at Dirac points $\mathbf{D}_i \in \{\mathbf{X}_1, \mathbf{X}_2, \mathbf{\Gamma}, \mathbf{M}\}$ with $\mathbf{X}_1 = (0, \pi)$, $\mathbf{X}_2 = (\pi, 0)$, $\mathbf{\Gamma} = (0, 0)$, and $\mathbf{M} = (\pi, \pi)$ for certain Zeeman coupling. When the system is fully gapped, the corresponding band topology can be characterized by the first Chern number Ch_1 , determining the QAH topological region $0 < |m_z| < 4t_0$ with $\text{Ch}_1 = \text{sgn}(m_z)$ and the trivial region $|m_z| > 4t_0$. This noninteracting topological property can also be captured by more intuitive and physical quantities, such as the spin textures on band inversion surfaces [76, 84] and spin polarizations on four Dirac points [58, 63].

The presence of nonzero interactions can greatly affect the physics of Hamiltonian (1) and may induce various interesting quantum phases at suitable interaction strength, such as the superfluid phase in attractive interaction [104, 105] and the antiferromagnetic phase in repulsive interaction [106, 107]. Especially for a general strong interaction, the system may host rich magnetic phases [108–110]. Yet, here we focus on the system at half filling [111] within a weak to intermediate interacting regime, where the interaction mainly induces ferromagnetic order. In this case, under the mean-field level the Hubbard interaction can be rewritten as

$$\sum_{\mathbf{j}} n_{\mathbf{j}\uparrow} n_{\mathbf{j}\downarrow} = n_{\uparrow} \sum_{\mathbf{k}} c_{\mathbf{k}\downarrow}^\dagger c_{\mathbf{k}\downarrow} + n_{\downarrow} \sum_{\mathbf{k}} c_{\mathbf{k}\uparrow}^\dagger c_{\mathbf{k}\uparrow} - N n_{\uparrow} n_{\downarrow} \quad (2)$$

with $n_s = (1/N) \sum_{\mathbf{k}} \langle c_{\mathbf{k}s}^\dagger c_{\mathbf{k}s} \rangle$. Here N is the total number of sites. It is clear that the nonzero interaction corrects the Zeeman coupling to an effective form

$$m_z^{\text{eff}} = m_z - U \frac{(n_{\uparrow} - n_{\downarrow})}{2} = m_z - U n_d, \quad (3)$$

where $n_d \equiv (n_{\uparrow} - n_{\downarrow})/2$ is the difference of density for spin-up and spin-down particles. The effective Zeeman coupling shifts the topological region to $0 < |m_z^{\text{eff}}| < 4t_0$ with $\text{Ch}_1 = \text{sgn}(m_z^{\text{eff}})$ in the interacting regime.

By self-consistently calculating the particle number density $n_{\uparrow(\downarrow)}$ [Figs. 1(a) and 1(b)], we show the mean-field phase diagram of QAH-Hubbard model (1) in Fig. 1(c). An important feature is that the topological phase boundaries depend on the strength of nonzero interaction and Zeeman coupling linearly [see Appendix A]. Indeed, this linear behavior of topological boundaries is essentially a natural consequence of the linear form of the contour lines of n_d in terms of the interaction strength and Zeeman coupling, as we show in Fig. 1(d). On these lines, m_z^{eff} is also unchanged, since n_d is fully determined by the effective Zeeman coupling. Specifically, we have $n_d^* = \pm 0.4068$ on the topological phase

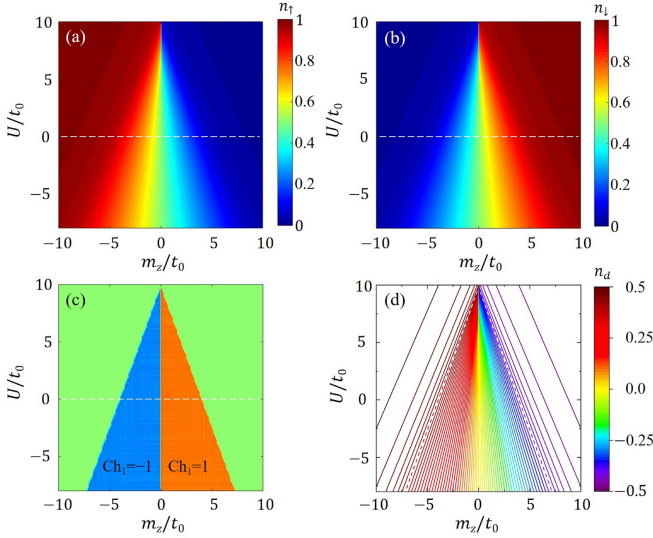


FIG. 1. (a)-(b) Self-consistent results of n_\uparrow and n_\downarrow . (c) Mean-field phase diagram for the nonzero U and m_z . (d) Contour lines of n_d , where the topological phase boundaries (two dashed lines) have $n_d^* = \pm 0.4068$. Here we set $t_{so} = t_0$ and $N = 60 \times 60$.

boundaries $|m_z^{\text{eff}}| = 4t_0$ for $t_{so} = t_0$. This linear scaling form of n_d also greatly affects the dynamical properties of the system and leads to novel phenomena in the quench dynamics.

III. QUENCH DYNAMICS

It is known that the quench dynamics has been widely used in cold atoms [59, 62, 82, 112]. The above mean-field topological phase diagram can be dynamically detected by employing the quantum quench scheme. Unlike the interaction quench in Refs. [96, 98], here we choose the Zeeman coupling as quench parameter, which has the following advantages: (i) The effective Zeeman coupling directly determines the topology of mean-field ground states at equilibrium. (ii) The Zeeman field in spin-orbit coupled quantum gases is controlled by the laser intensity and/or detuning and can be changed in a very short time scale, fulfilling the criterion for a sudden quench. (iii) The real experiments [113–115] have demonstrated that both the magnitude and the sign of Zeeman field can be tuned, which is more convenient to operate.

The quench protocol is as follows. We first initialize the system into a near fully polarized state for time $t < 0$ by taking a very large constant magnetization $m_z^{(c)}$ along the σ_z axis but a very small $m_{x(y)}^{(c)}$ along $\sigma_{x(y)}$ axis. In this case, the effect of interaction U can be ignored, and the spin of initial state is almost along the z axis with only a very small component in the x - y plane. At $t = 0$, we suddenly change the Zeeman coupling $m_z^{(c)}$ to the postquench value m_z and remove $m_{x(y)}^{(c)}$, then the near

fully polarized state begins to evolve under the equation of motion $i\dot{\Psi}_{\mathbf{k}}(t) = \mathcal{H}_{\mathbf{k}}(t)\Psi_{\mathbf{k}}(t)$ with

$$\mathcal{H}_{\mathbf{k}}(t) = \begin{bmatrix} h_{z,\mathbf{k}} + Un_\downarrow(t) & h_{x,\mathbf{k}} - ih_{y,\mathbf{k}} \\ h_{x,\mathbf{k}} + ih_{y,\mathbf{k}} & -h_{z,\mathbf{k}} + Un_\uparrow(t) \end{bmatrix}, \quad (4)$$

where $\Psi_{\mathbf{k}}(t) = [\chi_{\mathbf{k}}(t), \eta_{\mathbf{k}}(t)]^T$ is the instantaneous many-body state and $\mathcal{H}_{\mathbf{k}}(t)$ is the postquench Hamiltonian. To facilitate the capture of nontrivial properties in quantum dynamics, here $m_z^{(c)}$ should have the same sign as the postquench m_z .

Note that both the state $\Psi_{\mathbf{k}}(t)$ and Hamiltonian $\mathcal{H}_{\mathbf{k}}(t)$ are time-evolved, where the instantaneous particle number density is determined as

$$n_\uparrow(t) = \frac{1}{N} \sum_{\mathbf{k}} |\chi_{\mathbf{k}}(t)|^2, \quad n_\downarrow(t) = \frac{1}{N} \sum_{\mathbf{k}} |\eta_{\mathbf{k}}(t)|^2. \quad (5)$$

This is completely different from the noninteracting quantum quenches, where the postquench Hamiltonian keeps unchanged [76–81]. We note that even if the Hamiltonian $\mathcal{H}_{\mathbf{k}}(t)$ may become steady after the long time evolution, it is still different from the equilibrium mean-field Hamiltonian with the postquench parameter m_z and U , i.e.,

$$\mathcal{H}_{\mathbf{k}}^{\text{MF}} = \begin{bmatrix} h_{z,\mathbf{k}} - Un_d + \frac{U}{2} & h_{x,\mathbf{k}} - ih_{y,\mathbf{k}} \\ h_{x,\mathbf{k}} + ih_{y,\mathbf{k}} & -h_{z,\mathbf{k}} + Un_d + \frac{U}{2} \end{bmatrix}. \quad (6)$$

Here n_d is the equilibrium value. Hence the detection scheme for noninteracting topological phases is inapplicable in this case.

Next we shall propose a feasible dynamical scheme to detect the mean-field topological phases of $\mathcal{H}_{\mathbf{k}}^{\text{MF}}$ based on the above novel dynamical time evolution. By defining the time-evolved quantity $n_d(t) \equiv [n_\uparrow(t) - n_\downarrow(t)]/2$, we notice that the time-dependent effective Zeeman coupling

$$m_z^{\text{eff}}(t) = m_z - Un_d(t) \quad (7)$$

determines the topology $W(t)$ of the instantaneous postquench Hamiltonian $\mathcal{H}_{\mathbf{k}}(t)$ through the relation $W(t) = \text{sgn}[m_z^{\text{eff}}(t)]$ for $0 < |m_z^{\text{eff}}(t)| < 4t_0$ and $W(t) = 0$ otherwise. Since the equilibrium mean-field Hamiltonian $\mathcal{H}_{\mathbf{k}}^{\text{MF}}$ is actually determined by the self-consistent particle number density $n_{\uparrow(\downarrow)}$ (i.e., the equilibrium effective Zeeman coupling m_z^{eff} ; see the discussions in Sec. II), a key idea of identifying the equilibrium mean-field topological phases is to find a characteristic time t_s such that

$$n_{\uparrow(\downarrow)}(t_s) = n_{\uparrow(\downarrow)}. \quad (8)$$

Namely, the evolved particle number density $n_{\uparrow(\downarrow)}(t)$ at the time t_s captures the equilibrium self-consistent $n_{\uparrow(\downarrow)}$, giving the dynamical self-consistent particle number density $n_{\uparrow(\downarrow)}(t_s)$. Then the instantaneous Hamiltonian $\mathcal{H}_{\mathbf{k}}(t_s)$ is the same as the equilibrium mean-field Hamiltonian $\mathcal{H}_{\mathbf{k}}^{\text{MF}}$, and the time-dependent effective Zeeman coupling $m_z^{\text{eff}}(t_s)$ determines the corresponding

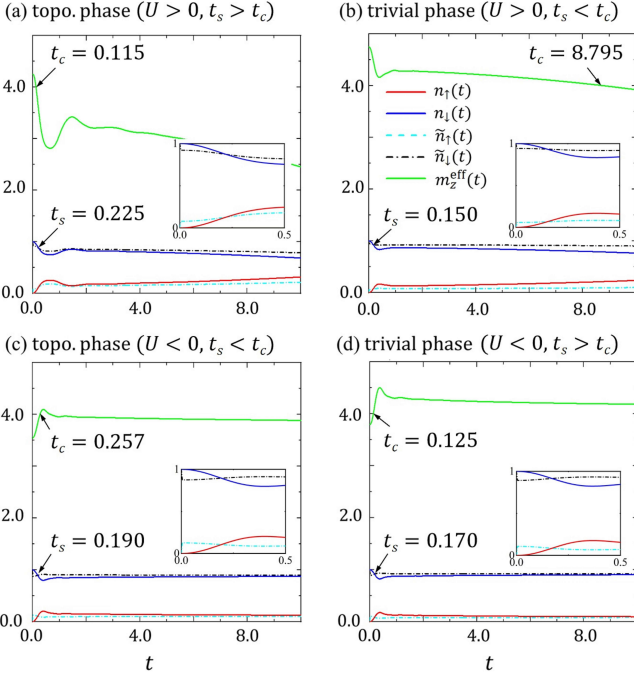


FIG. 2. Numerical results for $n_{\uparrow}(t)$ (red solid lines), $n_{\downarrow}(t)$ (blue solid lines), $m_z^{\text{eff}}(t)$ (green solid lines), $\tilde{n}_{\uparrow}(t)$ (light-blue dash-dotted lines), and $\tilde{n}_{\downarrow}(t)$ (black dash-dotted lines) for different interaction and equilibrium mean-field topological phases. Two characteristic time t_s and t_c emerge in the dynamical time evolution. Here the postquench parameters are $(m_z, U) = (1.4, 5.7)$, $(3.0, 3.5)$, $(4.9, -2.7)$, and $(5.8, -4.0)$ for (a)-(d), respectively. We set $t_{\text{so}} = t_0 = 1$, $m_x^{(c)} = m_z$, $m_y^{(c)} = 0$, and $m_z^{(c)} = 100$.

topology. We also introduce another characteristic time t_c such that

$$|m_z^{\text{eff}}(t_c)| = 4t_0, \quad (9)$$

characterizing the critical time of the dynamical topological phase transition of $\mathcal{H}_{\mathbf{k}}(t)$. Since Hamiltonian (6) behaves as a single particle model under mean-field level, $\mathcal{H}_{\mathbf{k}}(t_s)$ can essentially describe the ground state properties of the mean-field Hamiltonian $\mathcal{H}_{\mathbf{k}}^{\text{MF}}$ and its topological phase transition is obtained by $\mathcal{H}_{\mathbf{k}}(t_c)$. With this, identifying the topology of $\mathcal{H}_{\mathbf{k}}(t_s)$ as well as that of $\mathcal{H}_{\mathbf{k}}^{\text{MF}}$ is equivalent to comparing the characteristic time t_s and t_c in the quench dynamics [i.e., comparing $m_z^{\text{eff}}(t_s)$ and $m_z^{\text{eff}}(t_c)$].

In Fig. 2, we show the time evolution of $n_{\uparrow(\downarrow)}(t)$ and $m_z^{\text{eff}}(t)$ and confirm the existence of characteristic time t_s and t_c . Since the system is initially prepared in the near fully polarized state, the short-time evolution of $n_d(t)$ increases (decays) from $n_d(t=0) \approx -0.5$ ($+0.5$), when the postquench Zeeman coupling m_z is positive (negative). We also observe that the two characteristic time both emerge in the short-time evolution, and their relative relation ($t_s < t_c$ or $t_s > t_c$) behaves differently for different interaction and equilibrium mean-field phases.

In the following, we show how to identify the equilibrium mean-field topological phases via t_s and t_c in detail.

IV. NONTRIVIAL DYNAMICAL PROPERTIES

In this section, we determine the characteristic time t_s and t_c entirely from the quantum dynamics without knowing the postquench equilibrium mean-field value of $n_{\uparrow(\downarrow)}$, and provide the analytical results under certain conditions. The nontrivial dynamical properties in this interacting system are uncovered.

A. Dynamical self-consistent particle number density and characteristic time t_s

Since the equilibrium mean-field value of $n_{\uparrow(\downarrow)}$ is in general unknown, we need to first figure out how to determine the characteristic time t_s in the quantum dynamics. A notable fact is that $n_{\uparrow(\downarrow)}$ is self-consistently obtained for the mean-field Hamiltonian $\mathcal{H}_{\mathbf{k}}^{\text{MF}}$, and the time-evolved particle number density $n_{\uparrow(\downarrow)}(t)$ can be considered as a specific path for updating the mean-field parameters. For this, we introduce another set of time-dependent particle number density

$$\tilde{n}_{\uparrow}(t) = \frac{1}{N} \sum_{\mathbf{k}} |\tilde{\chi}_{\mathbf{k}}(t)|^2, \quad \tilde{n}_{\downarrow}(t) = \frac{1}{N} \sum_{\mathbf{k}} |\tilde{\eta}_{\mathbf{k}}(t)|^2 \quad (10)$$

for the eigenvector $\tilde{\Psi}_{\mathbf{k}}(t) = [\tilde{\chi}_{\mathbf{k}}(t), \tilde{\eta}_{\mathbf{k}}(t)]^T$ of $\mathcal{H}_{\mathbf{k}}(t)$ with negative energy, which can be obtained once we know the instantaneous particle number density $n_{\uparrow(\downarrow)}(t)$. We see that $\mathcal{H}_{\mathbf{k}}(t)$ is self-consistent when the two sets of time-dependent particle number density coincide, giving the characteristic time

$$t_s \equiv \min\{t | n_{\uparrow(\downarrow)}(t) = \tilde{n}_{\uparrow(\downarrow)}(t)\}, \quad (11)$$

at which we have $n_{\uparrow(\downarrow)} = n_{\uparrow(\downarrow)}(t_s) = \tilde{n}_{\uparrow(\downarrow)}(t_s)$, as shown in Fig. 2. This gives the dynamical self-consistent particle number density $n_{\uparrow(\downarrow)}(t_s)$, capturing the equilibrium self-consistent $n_{\uparrow(\downarrow)}$.

Note that here only the time-dependent particle number density becomes self-consistent, while the instantaneous wavefunction is in general not, which has subtle difference from the equilibrium mean-field Hamiltonian. This also implies that different instantaneous states may lead to the same $n_{\uparrow(\downarrow)}(t_s)$, and there may be multiple time points fulfilling the self-consistent condition. We hereby choose the smallest time point as the characteristic time t_s due to the consideration of short-time evolution [see Fig. 2(a)]. Also, the characteristic time t_s shall definitely appear in the short-time evolution, since the $n_{\uparrow(\downarrow)}(t)$ increases or decays in this regime and the state gradually reaches a steady state after $t > t_s$.

Although the explicit form of the characteristic time t_s is in general very complex, we can obtain an analytical

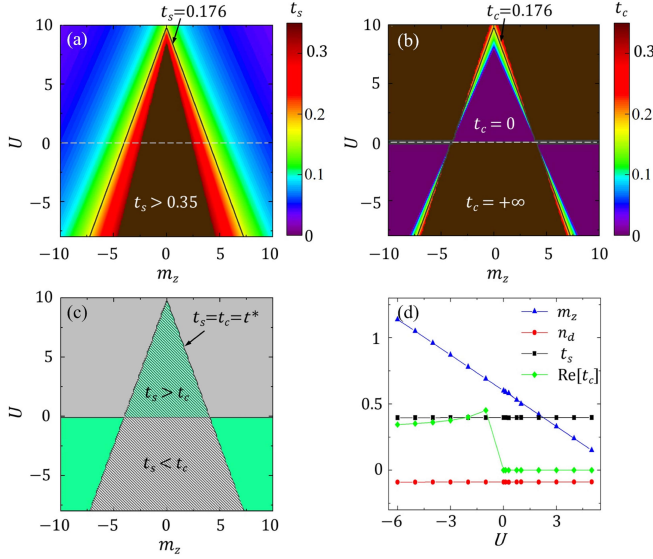


FIG. 3. (a)-(b) Analytical results of t_s and t_c , where $t^* = t_s = t_c = 0.176$ is on the topological boundaries (black solid lines). The dark-brown regions present $t_s > 0.35$ in (a) and $t_c = +\infty$ in (b) respectively, while the dark-purple regions in (b) give $t_c = 0$. These regions actually correspond to the complex values of t_s and t_c since a large truncation $\mathcal{O}(U^3 n_d^3)$ is taken. After reducing the truncation error, t_s gives the real value but t_c still gives complex value due to no solution. (c) Sign of $t_s - t_c$, where the shaded area is the equilibrium topological phase region. (d) Analytical results of t_s , n_d and $\text{Re}[t_c]$ at $n_d \approx -0.09$, showing the linear scaling of t_s and n_d . Here we set $t_{\text{so}} = t_0 = 1$.

result in the short-time evolution for a weak interaction strength U or $|Un_d|$, which is given by [see Appendix B]

$$t_s \approx \sqrt{\frac{N_1}{N_0 + \sqrt{N_2 + N_3(m_z - n_d U)^2}}} \quad (12)$$

with $N_0 = 12t_{\text{so}}^2$, $N_1 = 3(1 \pm 2n_d)$, $N_2 = -28t_{\text{so}}^4(\pm 10n_d - 1) - 72t_0^2 t_{\text{so}}^2(\pm 2n_d + 1)$, and $N_3 = -28t_{\text{so}}^2(\pm 2n_d + 1)$, where the symbol \pm corresponds to the sign of the postquench m_z . From this result, we observe that the characteristic time t_s is fixed by n_d . Since the contour lines of n_d have the linear form of interaction strength U and Zeeman coupling m_z , then t_s has a similar linear scaling, which fully matches with the numerical results [see Fig. 3(a)].

B. Dynamical topological phase transition and characteristic time t_c

We now determine the characteristic time t_c from the dynamical topological phase transition of $\mathcal{H}_{\mathbf{k}}(t)$. Since the initial state is prepared into a near fully polarized state for $t < 0$ and has $n_d(t = 0) \approx \pm 0.5$ for negative or positive postquench m_z , the absolute value of $n_d(t)$ in general decays in the time evolution and approaches a steady value. We find that when the interaction strength

satisfies $U > -8t_0$, the time-dependent effective Zeeman coupling $m_z^{\text{eff}}(t)$ passes through only one phase transition point $4t_0$ for $m_z > 0$ or $-4t_0$ for $m_z < 0$, although the corresponding crossing may occur multiple times. Therefore, $\mathcal{H}_{\mathbf{k}}(t)$ can only change from the trivial (topological) regime at $t = 0$ to the topological (trivial) regime for $t > 0$, when the interaction is repulsive (attractive). The characteristic time t_c , characterizing the critical time of the dynamical topological phase transition of $\mathcal{H}_{\mathbf{k}}(t)$, can be naturally defined as

$$t_c \equiv \min\{t | m_z^{\text{eff}}(t) = \pm 4t_0\} \quad (13)$$

Correspondingly, we have $t_c = +\infty$ and 0 ($t_c = 0$ and $+\infty$) in the repulsive (attractive) interaction regime for $|m_z^{\text{eff}}(t)| > 4t_0$ and $|m_z^{\text{eff}}(t)| < 4t_0$, respectively. The numerical results for $m_z > 0$ are shown in Fig. 2, where $m_z^{\text{eff}}(t)$ only passes through the phase transition point $m_z^{\text{eff}}(t_c) = 4t_0$ and decays (increases) for the repulsive (attractive) interaction in the short time region. This feature actually can be described by the analytical result for $n_d(t)$ in Appendix B, where we have $\dot{m}_z^{\text{eff}}(t) \gtrless 0$ for $Um_z \lesseqgtr 0$ due to $\dot{m}_z^{\text{eff}}(t) = -U\dot{n}_d(t)$.

Like Eq. (12), we can also obtain an analytical result for t_c in the short-time evolution [see Appendix B]:

$$t_c \approx \sqrt{\frac{P_0 - \sqrt{P_2 - 3P_1(\pm m_z - 4t_0)/U}}{P_1}} \quad (14)$$

with $P_0 = 6t_{\text{so}}^2$, $P_1 = 4t_{\text{so}}^2(5t_{\text{so}}^2 + 19t_0^2)$, and $P_2 = 6t_{\text{so}}^2(t_{\text{so}}^2 - 19t_0^2)$. Compared with t_s , the characteristic time t_c presents a completely different scaling form in terms of the Zeeman coupling and interaction strength, except for the topological phase boundaries [see Fig. 3(b)]. Particularly, the finite t_c only appears around the topological phase boundaries, since $\mathcal{H}_{\mathbf{k}}(t)$ always remains topological or trivial when it is far away from the phase boundaries; see Fig. 5(b).

C. Linear scaling of characteristic time on phase boundaries

We now give a special time t^* on the topological phase boundaries, which shows the linear scaling for the Zeeman coupling and interaction. By taking $m_z - Un_d = \pm 4t_0$ for the above two analytical characteristic time, we obtain

$$t^* = t_s = t_c \approx \sqrt{\frac{B_1}{B_0 + \sqrt{B_2}}}, \quad (15)$$

where $B_0 = 6t_{\text{so}}^2$, $B_1 = 3(1 \pm 2n_d^*)/2$, and $B_2 = -114(1 \pm 2n_d^*)t_0^2 t_{\text{so}}^2 - 6(\pm 10n_d^* - 1)t_{\text{so}}^4$; see Appendix B. This is a necessary condition for the topological transition of $\mathcal{H}_{\mathbf{k}}^{\text{MF}}$. Especially, we have $t^* \propto 1/t_0$ for a strong coupling with $t_{\text{so}} = t_0$, which gives $t^* = 0.176$ when $t_{\text{so}} = t_0 = 1$, matching the numerical result $t^* = 0.180$ [see Fig. 5(b)]. With the time t_s , t_c , and t^* , the equilibrium mean-field topological phases is next characterized.

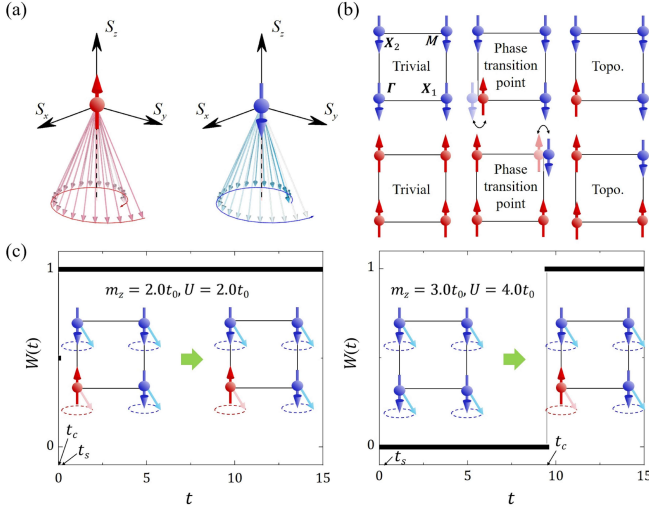


FIG. 4. (a) Schematic diagram for the motion of the near fully polarized spin at Dirac points \mathbf{D}_i . The clockwise (counterclockwise) motion of the spin implies the upward (downward) polarization of Hamiltonian at these points. (b) The polarization directions at Dirac points \mathbf{D}_i determine the topology of postquench Hamiltonian. (c) Topological number $W(t)$ for $\mathcal{H}_k(t)$. We have $\text{Ch}_1 = 1$ for the phase with $(m_z, U) = (2, 2)$ due to $t_c = 0 < t_s = 0.165$, while $\text{Ch}_1 = 0$ for the phase with $(m_z, U) = (3, 4)$ due to $t_c = 9.485 > t_s = 0.230$. The insets show the changes of polarization directions at Dirac points \mathbf{D}_i for $\mathcal{H}_k(t)$. Here we set $t_{so} = t_0 = 1$, $m_x^{(c)} = m_z$, $m_y^{(c)} = 0$, and $m_z^{(c)} = 100$.

V. DETERMINATION OF MEAN-FIELD TOPOLOGICAL PHASES

Based on the properties of $n_d(t)$ and $m_z^{\text{eff}}(t)$, the system shall have $t_s > t_c$ ($t_s < t_c$) in the quench dynamics for topological phases with the repulsive (attractive) interaction, if $\mathcal{H}_k(t)$ is trivial (topological) at $t = 0$. The correspondence between the characteristic time and the equilibrium topological properties is given by

$$|\text{Ch}_1| = \begin{cases} 1, & \text{for } \begin{cases} t_s > t^* > t_c, & U > 0 \\ t_s < t^* < t_c, & U < 0 \end{cases} \\ 0, & \text{for } \begin{cases} t^* < t_s < t_c, & U > 0 \\ t^* > t_s > t_c, & U < 0 \end{cases} \end{cases} \quad (16)$$

where t^* is for the gap closing at Dirac points Γ or M . The above formula provides a convenient method to determine the mean-field topological phase diagram by observing the short-time evolution of the system after quantum quench. Moreover, both the numerical results [Fig. 2] and the analytical results [Fig. 3(c)] confirm this scheme, especially for weak interaction U or small $|Un_d|$, as we show in Fig. 3(d).

To further determine the Chern number of the equilibrium mean-field topological phases, we consider the features of spin dynamics, which is described by the

modified Landau-Lifshitz equation in this interacting system [116]

$$\dot{\mathbf{S}}(\mathbf{k}, t) = \mathbf{S}(\mathbf{k}, t) \times 2\mathbf{h}(\mathbf{k}, t) \quad (17)$$

with

$$\begin{aligned} S_x(\mathbf{k}, t) &= [\chi_{\mathbf{k}}(t)\eta_{\mathbf{k}}^*(t) + \chi_{\mathbf{k}}^*(t)\eta_{\mathbf{k}}(t)]/2, \\ S_y(\mathbf{k}, t) &= i[\chi_{\mathbf{k}}(t)\eta_{\mathbf{k}}^*(t) - \chi_{\mathbf{k}}^*(t)\eta_{\mathbf{k}}(t)]/2, \\ S_z(\mathbf{k}, t) &= [|\chi_{\mathbf{k}}(t)|^2 - |\eta_{\mathbf{k}}(t)|^2]/2. \end{aligned} \quad (18)$$

We show in the following that the topology number $W(t)$ of the time-dependent postquench Hamiltonian $\mathcal{H}_k(t)$ can be determined by the dynamical properties of S_z at four Dirac points \mathbf{D}_i . The Chern number Ch_1 for mean-field Hamiltonian $\mathcal{H}_k^{\text{MF}}$ is then obtained by W at the characteristic time t_s .

First, for the near fully polarized initial state, the spin at Dirac points \mathbf{D}_i will move around the corresponding polarization direction of $\mathcal{H}_k(t)$ after the quantum quench. When the polarization direction is reversed, e.g., from upward to downward, the motion of spin will be reversed at the same time, e.g., from clockwise to counterclockwise; see Fig. 4(a). For this, we can use the motion of spins to determine the polarization direction of $\mathcal{H}_k(t)$ at Dirac points. Second, since the polarization direction is associated with the parity eigenvalue of the occupied eigenstate, the topology of $\mathcal{H}_k(t)$ can be identified from the polarization directions at four Dirac points [63], as shown in Fig. 4(b). For instance, the polarization directions at four Dirac points are the same for an initial trivial Hamiltonian $\mathcal{H}_k(t)$. Once it enters the topological regime, the motion of spin at Γ or M point will be reversed, manifesting the change of the corresponding polarization direction. This can be captured by the quantity $\text{sgn}[\dot{S}_z(\mathbf{D}_i, t)]$, as shown in Fig. 5(d). Based on the above points, we define the following time-dependent dynamical invariant for $\mathcal{H}_k(t)$:

$$(-1)^{\nu(t)} = \prod_i \text{sgn}[\dot{S}_z(\mathbf{D}_i, t)] \quad (19)$$

with $\nu(t) = 1$ for the topological regime $|m_z^{\text{eff}}(t)| < 4t_0$ and $\nu(t) = 0$ for the trivial regime $|m_z^{\text{eff}}(t)| > 4t_0$, respectively. With this, the topological number $W(t)$ of $\mathcal{H}_k(t)$ and the Chern number of $\mathcal{H}_k^{\text{MF}}$ can be exactly given as

$$W(t) = \frac{\nu(t)}{2} \sum_i \text{sgn}[\dot{S}_z(\mathbf{D}_i, t)], \quad \text{Ch}_1 = W(t_s). \quad (20)$$

As an example, the numerical results in Fig. 4(c) clearly show the nontrivial topology with $\text{Ch}_1 = 1$ and the trivial topology with $\text{Ch}_1 = 0$ for the postquench system with $(m_z, U) = (2, 2)$ and $(3, 4)$, respectively.

VI. EXPERIMENTAL DETECTION

Based on the above analysis of characteristic time, in this section we propose an experimentally feasible scheme to detect the mean-field topological phase diagram.

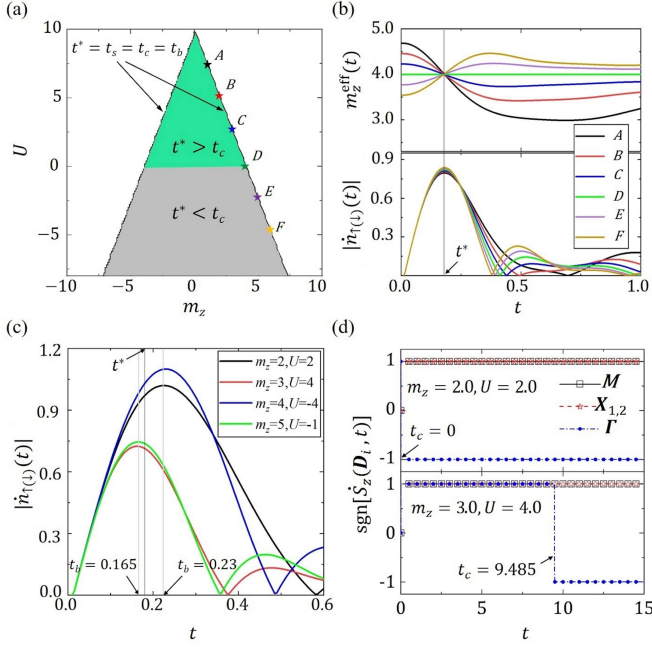


FIG. 5. (a) Mean-field phase diagram determined by the characteristic time t_c and t^* , where the postquench parameters $A-F$ (stars) are chosen on the topological phase boundaries with $(m_z, U) = (1.0, 7.38)$, $(2.0, 4.92)$, $(3.0, 2.46)$, $(4.0, 0)$, $(5.0, -2.46)$, and $(6.0, -4.92)$. (b) Dynamical evolution of $m_z^{\text{eff}}(t)$ and $|\dot{n}_{\uparrow(\downarrow)}(t)|$ for $A-F$, where $t_c = t^* = 0.180$ (upper) and $t_b = t^* = 0.180$ (lower) with the same scaling. (c) Dynamical evolution of $|\dot{n}_{\uparrow(\downarrow)}(t)|$, where $t_b = 0.165$ for $(m_z, U) = (3.0, 4.0)$ and $(5.0, -1.0)$ while $t_b = 0.230$ for $(m_z, U) = (2.0, 2.0)$ and $(4.0, -4.0)$. (d) Sign of $\dot{S}_z(\mathbf{D}_i, t)$ at four Dirac points. We have $\text{Ch}_1 = 1$ for the topological phase with $(m_z, U) = (2.0, 2.0)$ due to $t_c = 0 < t^*$ and $\text{Ch}_1 = 0$ for the trivial phase with $(m_z, U) = (3.0, 4.0)$ due to $t_c = 9.485 > t^*$. Here we set $t_{\text{so}} = t_0 = 1$, $m_x^{(c)} = m_z$, $m_y^{(c)} = 0$, and $m_z^{(c)} = 100$.

In real quench experiments, the characteristic time t_c can be directly detected from the spin dynamics by measuring $n_{\uparrow(\downarrow)}(t)$. The challenging part is how to measure the characteristic time t_s , since it does not have any measurable quantities but only corresponds to the self-consistent results of $\mathcal{H}_{\mathbf{k}}(t)$. To circumvent this difficulty, we instead choose to compare t^* and t_c based on Eq. (20) to detect the mean-field topological phase diagram; see Fig. 5(a). The time t^* can be directly measured by defining an auxiliary time

$$t_b \equiv \min\{t | \ddot{n}_{\uparrow(\downarrow)}(t) = 0\}, \quad (21)$$

at which the short-time evolution of $n_{\uparrow(\downarrow)}(t)$ changes fastest, i.e., $|\dot{n}_{\uparrow(\downarrow)}(t)|$ is maximal. Although the auxiliary time t_b is larger (smaller) than t^* in the topological (trivial) regime [see Fig. 5(c)], we indeed have $t_b = t^*$ on the topological phase boundaries, from which an analytical result for t^* is obtained as

$$t^* \approx \sqrt{\frac{3}{Q_0 + Q_1}} \quad (22)$$

with $Q_0 = \sqrt{-135t_0^2 + 606t_0^2t_{\text{so}}^2 + 57t_{\text{so}}^4}$ and $Q_1 = 57t_0^2 + 15t_{\text{so}}^2$, consistent with Eq. (15). Particularly, we have $t^* \approx 0.178$ for $t_0 = t_{\text{so}} = 1$. The auxiliary time t_b simplifies the detection of the mean-field topological phase diagram.

The dynamical detection scheme is as follows. First, due to the linear scaling of t^* in terms of U and m_z [see Fig. 3(c)], which is fixed on the mean-field topological phase boundaries, we can determine the special time t^* from the noninteracting ($U = 0$) quench dynamics. In this case, the Zeeman coupling is quenched from a large $m_z^{(c)}$ and a small $m_x^{(c)}$ to the postquench parameters on phase boundaries, i.e., $m_z = \pm 4t_0$ and $m_x(y) = 0$. Then the time-dependent particle number density $n_{\uparrow(\downarrow)}(t)$ in the short-time evolution is measured. By examining $\dot{n}_{\uparrow(\downarrow)}(t)$, we obtain $t^* = t_b$. Second, we turn to the interacting quench dynamics with postquench m_z to obtain the fully mean-field phase diagram. Here $m_x^{(c)}$ remains to be small and $m_x(y) = 0$. By measuring t_c from the quantum dynamics, the mean-field topological phase diagram is obtained by comparing it with t^* ; see Fig. 5(a). Finally, the Chern number of mean-field topological phases can also be obtained via Eq. (20). Since there is only one topological phase transition point, the topological number $W(t)$ has the same value at t_s and t^* . Hence we have

$$\text{Ch}_1 \simeq W(t^*). \quad (23)$$

With this scheme, the mean-field phase diagram of the interacting Chern insulator can be completely determined, which paves the way to experimentally study topological phases in interacting systems and discover new phases.

VII. CONCLUSION AND DISCUSSION

In conclusion, we have studied the 2D QAH model with a weak-to-intermediate Hubbard interaction by performing quantum quenches. A nonequilibrium detection scheme for the mean-field topological phase diagram is proposed by observing the characteristic time t_s and t_c , which capture the emergence of dynamical self-consistent particle number density and dynamical topological phase transition for the time-dependent postquench Hamiltonian, respectively. Two nontrivial dynamical properties are further uncovered. (i) After quenching the Zeeman coupling from the trivial regime to the topological regime, $t_s > t_c$ ($t_s < t_c$) is observed for the repulsive (attractive) interaction, and $t_s = t_c$ occurs on the topological phase boundaries. (ii) The Chern number of the postquench mean-field topological phase can be determined by the spin dynamics of four Dirac points at characteristic time t_s . Our results provide feasible schemes to identify the mean-field topological phases in an interacting Chern insulator and can be applied to quantum simulation experiments in the near future.

The present dynamical scheme can be applied to the Chern insulator with the weak-to-intermediate interac-

tion. On the other hand, when the general strong interactions are considered, the system may host more abundant magnetic phases [108–110]. Generalizing these dynamical properties to the related studies and further identifying the rich topological phases would be an interesting and worthwhile work in the future.

ACKNOWLEDGEMENT

We acknowledge the valuable discussions with Sen Niu and Ting Fung Jeffrey Poon. This work was supported by National Natural Science Foundation of China (Grants No. 11825401 and No. 11921005), the National Key R&D Program of China (Project No. 2021YFA1400900), Strategic Priority Research Program of the Chinese Academy of Science (Grant No. XDB28000000), and by the Open Project of Shenzhen Institute of Quantum Science and Engineering (Grant No. SIQSE202003). Lin Zhang also acknowledges support from Agencia Estatal de Investigación (the R&D project CEX2019-000910-S, funded by MCIN/AEI/10.13039/501100011033, Plan National FIDEUA PID2019-106901GB-I00, FPI), Fundació Privada Cellex, Fundació Mir-Puig, and Generalitat de Catalunya (AGAUR Grant No. 2017 SGR 1341, CERCA program).

Appendix A: Equilibrium analytical results

In presence of the non-zero interaction, the equilibrium mean-field Hamiltonian $\mathcal{H}_{\mathbf{k}}^{\text{MF}}$ self-consistently gives

$$n_d = \frac{1}{N} \sum_{\mathbf{k}} \frac{-h_{z,\mathbf{k}} + Un_d}{2\sqrt{h_{x,\mathbf{k}}^2 + h_{y,\mathbf{k}}^2 + (h_{z,\mathbf{k}} - Un_d)^2}}. \quad (\text{A1})$$

Considering that $|n_d| < 0.5$ is a small value due to $n_{\uparrow} + n_{\downarrow} = 1$, we use Taylor series at $n_d = 0$ for the right-hand term of Eq. (A1), which approximately gives $A_0 + A_1Un_d + A_2U^2n_d^2 + \dots + A_lU^ln_d^l$ with $(l+1)$ th-order truncation $\mathcal{O}(U^{l+1}n_d^{l+1})$. Here the coefficients $A_{i=0,1,\dots,l}$ satisfy $\partial A_0/\partial h_{z,\mathbf{k}} = -A_1$, $\partial A_1/\partial h_{z,\mathbf{k}} = -2A_2$, $\partial A_2/\partial h_{z,\mathbf{k}} = -3A_3, \dots$. We can obtain n_d by solving $n_d \approx A_0 + A_1Un_d + A_2U^2n_d^2 + \dots + A_lU^ln_d^l$, and the analytical n_d for $l = 2$ at a weak interaction or a small Zeeman coupling is given by

$$n_d \approx \frac{2 - A_1U - \sqrt{(2 - A_1U)^2 - 4A_0A_2U^2}}{2A_2U^2}, \quad (\text{A2})$$

with $A_0 = \frac{1}{N} \sum_{\mathbf{k}} \frac{-h_{z,\mathbf{k}}}{e_{\mathbf{k}}}$, $A_1 = \frac{1}{N} \sum_{\mathbf{k}} \frac{h_{x,\mathbf{k}}^2 + h_{y,\mathbf{k}}^2}{e_{\mathbf{k}}^3}$, and $A_2 = \frac{1}{N} \sum_{\mathbf{k}} \frac{3(h_{x,\mathbf{k}}^2 + h_{y,\mathbf{k}}^2)h_{z,\mathbf{k}}}{2e_{\mathbf{k}}^5}$. The Eq. (A2) shows the scaling property of n_d for the Zeeman coupling and interaction.

Besides, we observe that A_i can converge to zero for an increased i , as shown in Fig. 6(a). For the 3rd-order

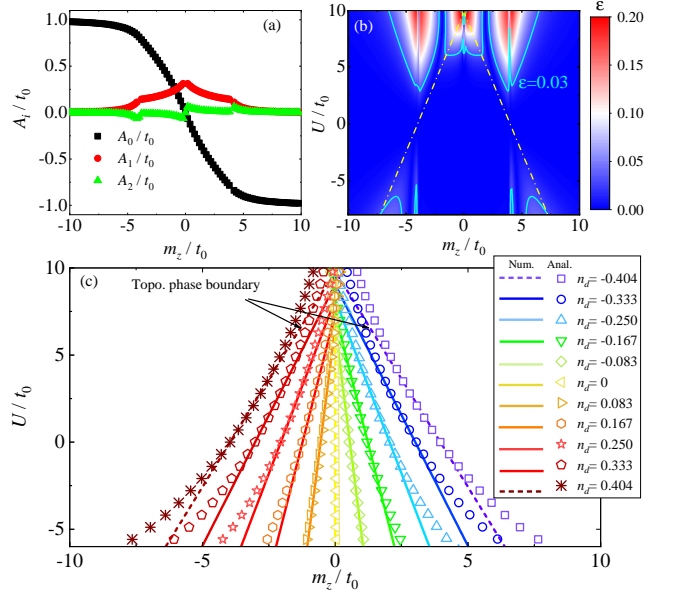


FIG. 6. (a) Analytical coefficients A_0 , A_1 , and A_2 . (b) Absolute error ϵ between the analytical results and the numerical results for n_d . (c) Analytical results of n_d corresponding to the numerical results shown in Fig. 1(d), giving the linear scaling. Here we set $t_{\text{so}} = t_0$.

truncation $\mathcal{O}(U^3n_d^3)$ in Eq. (A2), the absolute error ϵ between analytical and numerical results presents $\epsilon < 0.03$ for $|U| < 6t_0$, which implies that the precision of 3rd-order truncation is enough. It should be emphasized that Eq. (A2) is applicable to the almost completely topological phase region, all the topological boundaries, and a large trivial regions, as shown in Fig. 6(b). Also, the analytical results are almost confirmed with the numerical results for both a weak interaction or a small Zeeman coupling, as shown in Fig. 6(c).

Appendix B: Nonequilibrium analytical results

Considering that the spin of initial state is near fully polarized to downward or upward, we can take $[\chi_{\mathbf{k}}(0), \eta_{\mathbf{k}}(0)]^T \approx (0, 1)^T$ or $[\chi_{\mathbf{k}}(0), \eta_{\mathbf{k}}(0)]^T \approx (1, 0)^T$, which corresponds to the postquenched $m_z > 0$ or $m_z < 0$. Further, the change of $n_d(t)$ is small during a short-time evolution and it can be regarded as a constant in a very short time. By solving Eq. (4), we can obtain $n_d(t) \approx n_{d,t}$, given by

$$n_{d,t} = \pm \frac{1}{N} \sum_{\mathbf{k}} \frac{-e_{\mathbf{k},t}^2 + (h_{x,\mathbf{k}}^2 + h_{y,\mathbf{k}}^2)(1 - \cos 2te_{\mathbf{k},t})}{2e_{\mathbf{k},t}^2}, \quad (\text{B1})$$

where $e_{\mathbf{k},t} = \sqrt{h_{x,\mathbf{k}}^2 + h_{y,\mathbf{k}}^2 + (h_{z,\mathbf{k}} - n_{d,t}U)^2}$ and \pm still corresponds to the sign of the postquenched m_z . Similarly, we use Taylor series at $n_{d,t} = 0$ for the right-hand term of Eq. (B1), which approximately gives $D_0 +$

$D_1 U n_{d,t} + D_2 U^2 n_{d,t}^2 + \dots + D_l U^l n_{d,t}^l$ with $(l+1)$ th-order truncation $\mathcal{O}(U^{l+1} n_{d,t}^{l+1})$.

We further take the 3rd-order truncation $\mathcal{O}(U^3 n_{d,t}^3)$ to obtain the simple solution of $n_{d,t}$ as follows:

$$n_{d,t} \approx \frac{2 - D_1 U - \sqrt{(2 - D_1 U)^2 - 4 D_0 D_2 U^2}}{2 D_2 U^2} \quad (\text{B2})$$

with $D_0 = \pm 8 t_{\text{so}}^2 t^2 - [\pm 1 \pm 8 t_{\text{so}}^2 (m_z^2 + 3 t_0^2 + 5 t_{\text{so}}^2) t^4 / 3]$, $D_1 = \pm 16 m_z t_{\text{so}}^2 t^4 / 3$, and $D_2 = -(\pm 8 t_{\text{so}}^2 t^4 / 3)$. Note that we hereby have used Taylor series at $t = 0$ for $D_{0,1,2}$ and have taken 6th-order truncation $\mathcal{O}(t^6)$, and then this approximate $n_{d,t}$ is only suitable for a very short-time evolution or a small value of $|U n_{d,t}|$. Finally, we can explicitly give t_s , t_c , and t_b by solving $n_{d,t} = n_d$, $m_z - U n_{d,t} = \pm 4 t_0$, and $\dot{n}_{d,t} = 0$ respectively, where the explicit results are shown in Eq. (12), Eq. (14), and Eq. (22).

-
- [1] K. v. Klitzing, G. Dorda, and M. Pepper, New method for high-accuracy determination of the fine-structure constant based on quantized Hall resistance, *Phys. Rev. Lett.* **45**, 494 (1980).
 - [2] D. C. Tsui, H. L. Stormer, and A. C. Gossard, Two-dimensional magnetotransport in the extreme quantum limit, *Phys. Rev. Lett.* **48**, 1559 (1982).
 - [3] M. Z. Hasan and C. L. Kane, Colloquium: topological insulators, *Rev. Mod. Phys.* **82**, 3045 (2010).
 - [4] X.-G. Wen, Colloquium: Zoo of quantum-topological phases of matter, *Rev. Mod. Phys.* **89**, 041004 (2017).
 - [5] J. M. Kosterlitz, Nobel lecture: topological defects and phase transitions, *Rev. Mod. Phys.* **89**, 040501 (2017).
 - [6] X.-G. Wen, Topological orders in rigid states, *Int. J. of Mod. Phys. B* **4**, 239 (1990).
 - [7] X.-L. Qi and S.-C. Zhang, Topological insulators and superconductors, *Rev. Mod. Phys.* **83**, 1057 (2011).
 - [8] L. Fu, C. L. Kane, and E. J. Mele, Topological insulators in three dimensions, *Phys. Rev. Lett.* **98**, 106803 (2007).
 - [9] L. Fu and C. L. Kane, Topological insulators with inversion symmetry, *Phys. Rev. B* **76**, 045302 (2007).
 - [10] L. Fu, Topological crystalline insulators, *Phys. Rev. Lett.* **106**, 106802 (2011).
 - [11] C.-Z. Chang, J. Zhang, X. Feng, J. Shen, Z. Zhang, M. Guo, K. Li, Y. Ou, P. Wei, L.-L. Wang, Z.-Q. Ji, Y. Feng, S. Ji, X. Chen, J. Jia, X. Dai, Z. Fang, S.-C. Zhang, K. He, Y. Wang, L. Lu, X.-C. Ma, and Q.-K. Xue, Experimental observation of the quantum anomalous Hall effect in a magnetic topological insulator, *Science* **340**, 167 (2013).
 - [12] A. A. Burkov and L. Balents, Weyl semimetal in a topological insulator multilayer, *Phys. Rev. Lett.* **107**, 127205 (2011).
 - [13] S. M. Young, S. Zaheer, J. C. Y. Teo, C. L. Kane, E. J. Mele, and A. M. Rappe, Dirac semimetal in three dimensions, *Phys. Rev. Lett.* **108**, 140405 (2012).
 - [14] S.-Y. Xu, I. Belopolski, N. Alidoust, M. Neupane, G. Bian, C. Zhang, R. Sankar, G. Chang, Z. Yuan, C.-C. Lee, S.-M. Huang, H. Zheng, J. Ma, D. S. Sanchez, B. Wang, A. Bansil, F. Chou, P. P. Shibayev, H. Lin, S. Jia, and M. Z. Hasan, Discovery of a Weyl fermion semimetal and topological Fermi arcs, *Science* **349**, 613 (2015).
 - [15] B. Q. Lv, H. M. Weng, B. B. Fu, X. P. Wang, H. Miao, J. Ma, P. Richard, X. C. Huang, L. X. Zhao, G. F. Chen, Z. Fang, X. Dai, T. Qian, and H. Ding, Experimental discovery of Weyl semimetal TaAs, *Phys. Rev. X* **5**, 031013 (2015).
 - [16] X.-L. Qi, T. L. Hughes, S. Raghu, and S.-C. Zhang, Time-reversal-invariant topological superconductors and superfluids in two and three dimensions, *Phys. Rev. Lett.* **102**, 187001 (2009).
 - [17] B. A. Bernevig and T. L. Hughes, *Topological insulators and topological superconductors* (Princeton university press, 2013).
 - [18] Y. Ando and L. Fu, Topological crystalline insulators and topological superconductors: From concepts to materials, *Annu. Rev. Condens. Matter Phys.* **6**, 361 (2015).
 - [19] M. Sato and Y. Ando, Topological superconductors: a review, *Rep. Prog. Phys.* **80**, 076501 (2017).
 - [20] P. Zhang, K. Yaji, T. Hashimoto, Y. Ota, T. Kondo, K. Okazaki, Z. Wang, J. Wen, G. Gu, H. Ding, and S. Shin, Observation of topological superconductivity on the surface of an iron-based superconductor, *Science* **360**, 182 (2018).
 - [21] Z. Wang, X.-L. Qi, and S.-C. Zhang, Topological order parameters for interacting topological insulators, *Phys. Rev. Lett.* **105**, 256803 (2010).
 - [22] D. Pesin and L. Balents, Mott physics and band topology in materials with strong spin-orbit interaction, *Nat. Phys.* **6**, 376 (2010).
 - [23] D.-H. Lee, Effects of interaction on quantum spin Hall insulators, *Phys. Rev. Lett.* **107**, 166806 (2011).
 - [24] E. V. Castro, A. G. Grushin, B. Valenzuela, M. A. H. Vozmediano, A. Cortijo, and F. de Juan, Topological fermi liquids from coulomb interactions in the doped honeycomb lattice, *Phys. Rev. Lett.* **107**, 106402 (2011).
 - [25] M. A. N. Araújo, E. V. Castro, and P. D. Sacramento, Change of an insulator's topological properties by a Hubbard interaction, *Phys. Rev. B* **87**, 085109 (2013).
 - [26] H. Yao and S. Ryu, Interaction effect on topological classification of superconductors in two dimensions, *Phys. Rev. B* **88**, 064507 (2013).
 - [27] M. Messer, R. Desbuquois, T. Uehlinger, G. Jotzu, S. Huber, D. Greif, and T. Esslinger, Exploring competing density order in the ionic Hubbard model with ultracold fermions, *Phys. Rev. Lett.* **115**, 115303 (2015).
 - [28] S. Rachel, Interacting topological insulators: a review, *Rep. Prog. Phys.* **81**, 116501 (2018).
 - [29] O. Viyuela, L. Fu, and M. A. Martin-Delgado, Chiral topological superconductors enhanced by long-range interactions, *Phys. Rev. Lett.* **120**, 017001 (2018).
 - [30] A. Mook, K. Plekhanov, J. Klinovaja, and D. Loss, Interaction-stabilized topological magnon insulator in ferromagnets, *Phys. Rev. X* **11**, 021061 (2021).
 - [31] S. Raghu, X.-L. Qi, C. Honerkamp, and S.-C. Zhang, Topological Mott Insulators, *Phys. Rev. Lett.* **100**,

- 156401 (2008).
- [32] S. Rachel and K. Le Hur, Topological insulators and Mott physics from the Hubbard interaction, *Phys. Rev. B* **82**, 075106 (2010).
 - [33] T. I. Vanhala, T. Siro, L. Liang, M. Troyer, A. Harju, and P. Törmä, Topological phase transitions in the repulsively interacting Haldane-Hubbard model, *Phys. Rev. Lett.* **116**, 225305 (2016).
 - [34] X.-L. Qi, Y.-S. Wu, and S.-C. Zhang, Topological quantization of the spin hall effect in two-dimensional paramagnetic semiconductors, *Phys. Rev. B* **74**, 085308 (2006).
 - [35] X.-L. Qi, T. L. Hughes, and S.-C. Zhang, Chiral topological superconductor from the quantum Hall state, *Phys. Rev. B* **82**, 184516 (2010).
 - [36] X.-J. Liu, K. T. Law, and T. K. Ng, Realization of 2D spin-orbit interaction and exotic topological orders in cold atoms, *Phys. Rev. Lett.* **112**, 086401 (2014).
 - [37] Ting Fung Jeffrey Poon and X.-J. Liu, From a semimetal to a chiral Fulde-Ferrell superfluid, *Phys. Rev. B* **97**, 020501(R) (2018).
 - [38] W. Hofstetter and T. Qin, Quantum simulation of strongly correlated condensed matter systems, *J. Phys. B* **51**, 082001 (2018).
 - [39] B. Fauseweh and J.-X. Zhu, Digital quantum simulation of non-equilibrium quantum many-body systems, *Quant. Info. Proc.* **20**, 1 (2021).
 - [40] C. Monroe, W. C. Campbell, L.-M. Duan, Z.-X. Gong, A. V. Gorshkov, P. W. Hess, R. Islam, K. Kim, N. M. Linke, G. Pagano, P. Richerme, C. Senko, and N. Y. Yao, Programmable quantum simulations of spin systems with trapped ions, *Rev. Mod. Phys.* **93**, 025001 (2021).
 - [41] I. Bloch, J. Dalibard, and W. Zwerger, Many-body physics with ultracold gases, *Rev. Mod. Phys.* **80**, 885 (2008).
 - [42] T. Langen, R. Geiger, and J. Schmiedmayer, Ultracold atoms out of equilibrium, *Annu. Rev. Condens. Matter Phys.* **6**, 201 (2015).
 - [43] C. Gross and I. Bloch, Quantum simulations with ultracold atoms in optical lattices, *Science* **357**, 995 (2017).
 - [44] M. Schreiber, S. S. Hodgman, P. Bordia, H. P. Lüschen, M. H. Fischer, R. Vosk, E. Altman, U. Schneider, and I. Bloch, Observation of many-body localization of interacting fermions in a quasirandom optical lattice, *Science* **349**, 842 (2015).
 - [45] J. Smith, A. Lee, P. Richerme, B. Neyenhuis, P. W. Hess, P. Hauke, M. Heyl, D. A. Huse, and C. Monroe, Many-body localization in a quantum simulator with programmable random disorder, *Nat. Phys.* **12**, 907 (2016).
 - [46] P. Bordia, H. P. Lüschen, S. S. Hodgman, M. Schreiber, I. Bloch, and U. Schneider, Coupling identical one-dimensional many-body localized systems, *Phys. Rev. Lett.* **116**, 140401 (2016).
 - [47] J.-y. Choi, S. Hild, J. Zeiher, P. Schauß, A. Rubio-Abadal, T. Yefsah, V. Khemani, D. A. Huse, I. Bloch, and C. Gross, Exploring the many-body localization transition in two dimensions, *Science* **352**, 1547 (2016).
 - [48] V. V. Ramasesh, E. Flurin, M. Rudner, I. Siddiqi, and N. Y. Yao, Direct probe of topological invariants using Bloch oscillating quantum walks, *Phys. Rev. Lett.* **118**, 130501 (2017).
 - [49] Z. Jiang, K. J. Sung, K. Kechedzhi, V. N. Smelyanskiy, and S. Boixo, Quantum algorithms to simulate many-body physics of correlated fermions, *Phys. Rev. Applied* **9**, 044036 (2018).
 - [50] Z. Yan, Y.-R. Zhang, M. Gong, Y. Wu, Y. Zheng, S. Li, C. Wang, F. Liang, J. Lin, Y. Xu, C. Guo, L. Sun, C.-Z. Peng, K. Xia, H. Deng, H. Rong, J. Q. You, F. Nori, H. Fan, X. Zhu, and J.-W. Pan, Strongly correlated quantum walks with a 12-qubit superconducting processor, *Science* **364**, 753 (2019).
 - [51] W. P. Su, J. R. Schrieffer, and A. J. Heeger, Soliton excitations in polyacetylene, *Phys. Rev. B* **22**, 2099 (1980).
 - [52] M. Atala, M. Aidelsburger, J. T. Barreiro, D. Abanin, T. Kitagawa, E. Demler, and I. Bloch, Direct measurement of the Zak phase in topological Bloch bands, *Nat. Phys.* **9**, 795 (2013).
 - [53] X.-J. Liu, Z.-X. Liu, and M. Cheng, Manipulating topological edge spins in a one-dimensional optical lattice, *Phys. Rev. Lett.* **110**, 076401 (2013).
 - [54] B. Song, L. Zhang, C. He, T. F. J. Poon, E. Hagiye, S. Zhang, X.-J. Liu, and G.-B. Jo, Observation of symmetry-protected topological band with ultracold fermions, *Sci. Adv.* **4**, eaao4748 (2018).
 - [55] F. D. M. Haldane, Continuum dynamics of the 1-D Heisenberg antiferromagnet: Identification with the O(3) nonlinear sigma model, *Phys. Lett. A* **93**, 464 (1983).
 - [56] S. de Léséleuc, V. Lienhard, P. Scholl, D. Barredo, S. Weber, N. Lang, H. P. Büchler, T. Lahaye, and A. Browaeys, Observation of a symmetry-protected topological phase of interacting bosons with Rydberg atoms, *Science* **365**, 775 (2019).
 - [57] G. Jotzu, M. Messer, R. Desbuquois, M. Lebrat, T. Uehlinger, D. Greif, and T. Esslinger, Experimental realization of the topological Haldane model with ultracold fermions, *Nature* **515**, 237 (2014).
 - [58] Z. Wu, L. Zhang, W. Sun, X.-T. Xu, B.-Z. Wang, S.-C. Ji, Y. Deng, S. Chen, X.-J. Liu, and J.-W. Pan, Realization of two-dimensional spin-orbit coupling for Bose-Einstein condensates, *Science* **354**, 83 (2016).
 - [59] W. Sun, B.-Z. Wang, X.-T. Xu, C.-R. Yi, L. Zhang, Z. Wu, Y. Deng, X.-J. Liu, S. Chen, and J.-W. Pan, Highly controllable and robust 2D spin-orbit coupling for quantum gases, *Phys. Rev. Lett.* **121**, 150401 (2018).
 - [60] M.-C. Liang, Y.-D. Wei, L. Zhang, X.-J. Wang, H. Zhang, W.-W. Wang, W. Qi, X.-J. Liu, and X. Zhang, Realization of Qi-Wu-Zhang model in spin-orbit-coupled ultracold fermions, *arXiv:2109.08885*.
 - [61] W.-Y. He, S. Zhang, and K. T. Law, Realization and detection of Weyl semimetals and the chiral anomaly in cold atomic systems, *Phys. Rev. A* **94**, 013606 (2016).
 - [62] Z.-Y. Wang, X.-C. Cheng, B.-Z. Wang, J.-Y. Zhang, Y.-H. Lu, C.-R. Yi, S. Niu, Y. Deng, X.-J. Liu, S. Chen, and J.-W. Pan, Realization of an ideal Weyl semimetal band in a quantum gas with 3D spin-orbit coupling, *Science* **372**, 271 (2021).
 - [63] X.-J. Liu, K.-T. Law, T.-K. Ng, and P. A. Lee, Detecting topological phases in cold atoms, *Phys. Rev. Lett.* **111**, 120402 (2013).
 - [64] M. Hafezi, Measuring topological invariants in photonic systems, *Phys. Rev. Lett.* **112**, 210405 (2014).
 - [65] J. Wu, J. Liu, and X.-J. Liu, Topological spin texture in a quantum anomalous Hall insulator, *Phys. Rev. Lett.* **113**, 136403 (2014).
 - [66] H. M. Price, O. Zilberberg, T. Ozawa, I. Carusotto, and N. Goldman, Measurement of Chern numbers through

- center-of-mass responses, *Phys. Rev. B* **93**, 245113 (2016).
- [67] S. Vajna and B. Dóra, Topological classification of dynamical phase transitions, *Phys. Rev. B* **91**, 155127 (2015).
- [68] Y. Hu, P. Zoller, and J. C. Budich, Dynamical buildup of a quantized hall response from nontopological states, *Phys. Rev. Lett.* **117**, 126803 (2016).
- [69] J. C. Budich and M. Heyl, Dynamical topological order parameters far from equilibrium, *Phys. Rev. B* **93**, 085416 (2016).
- [70] J. H. Wilson, J. C. W. Song, and G. Refael, Remnant geometric Hall response in a quantum quench, *Phys. Rev. Lett.* **117**, 235302 (2016).
- [71] M. Heyl, Dynamical quantum phase transitions: a review, *Rep. Prog. Phys.* **81**, 054001 (2018).
- [72] H. Hu, B. Huang, E. Zhao, and W. V. Liu, Dynamical singularities of floquet higher-order topological insulators, *Phys. Rev. Lett.* **124**, 057001 (2020).
- [73] H. Hu and E. Zhao, Topological invariants for quantum quench dynamics from unitary evolution, *Phys. Rev. Lett.* **124**, 160402 (2020).
- [74] W.-T. Kuo, D. Arovass, S. Vishveshwara, and Y.-Z. You, Decoherent quench dynamics across quantum phase transitions, *SciPost Phys.* **11**, 084 (2021).
- [75] D.-H. Cai and W. Yi, Synthetic topology and floquet dynamic quantum phase transition in a periodically driven raman lattice, *Phys. Rev. A* **105**, 042812 (2022).
- [76] L. Zhang, L. Zhang, S. Niu, and X.-J. Liu, Dynamical classification of topological quantum phases, *Sci. Bull.* **63**, 1385 (2018).
- [77] L. Zhang, L. Zhang, and X.-J. Liu, Characterizing topological phases by quantum quenches: A general theory, *Phys. Rev. A* **100**, 063624 (2019).
- [78] J. Ye and F. Li, Emergent topology under slow nonadiabatic quantum dynamics, *Phys. Rev. A* **102**, 042209 (2020).
- [79] W. Jia, L. Zhang, L. Zhang, and X.-J. Liu, Dynamically characterizing topological phases by high-order topological charges, *Phys. Rev. A* **103**, 052213 (2021).
- [80] L. Li, W. Zhu, and J. Gong, Direct dynamical characterization of higher-order topological phases with nested band inversion surfaces, *Sci. Bull.* **66**, 1502 (2021).
- [81] L. Zhang, W. Jia, and X.-J. Liu, Universal topological quench dynamics for \mathbb{Z}_2 topological phases, *Sci. Bull.* **67**, 1236 (2022).
- [82] W. Sun, C.-R. Yi, B.-Z. Wang, W.-W. Zhang, B. C. Sanders, X.-T. Xu, Z.-Y. Wang, J. Schmiedmayer, Y. Deng, X.-J. Liu, S. Chen, and J.-W. Pan, Uncover topology by quantum quench dynamics, *Phys. Rev. Lett.* **121**, 250403 (2018).
- [83] M. Tarnowski, F. N. Ünal, N. Fläschner, B. S. Rem, A. Eckardt, K. Sengstock, and C. Weitenberg, Measuring topology from dynamics by obtaining the Chern number from a linking number, *Nat. Commun.* **10**, 1 (2019).
- [84] C.-R. Yi, L. Zhang, L. Zhang, R.-H. Jiao, X.-C. Cheng, Z.-Y. Wang, X.-T. Xu, W. Sun, X.-J. Liu, S. Chen, and J.-W. Pan, Observing topological charges and dynamical bulk-surface correspondence with ultracold atoms, *Phys. Rev. Lett.* **123**, 190603 (2019).
- [85] Y. Wang, W. Ji, Z. Chai, Y. Guo, M. Wang, X. Ye, P. Yu, L. Zhang, X. Qin, P. Wang, F. Shi, X. Rong, D. Lu, X.-J. Liu, and J. Du, Experimental observation of dynamical bulk-surface correspondence in momentum space for topological phases, *Phys. Rev. A* **100**, 052328 (2019).
- [86] T. Xin, Y. Li, Y.-a. Fan, X. Zhu, Y. Zhang, X. Nie, J. Li, Q. Liu, and D. Lu, Quantum Phases of Three-Dimensional Chiral Topological Insulators on a Spin Quantum Simulator, *Phys. Rev. Lett.* **125**, 090502 (2020).
- [87] W. Ji, L. Zhang, M. Wang, L. Zhang, Y. Guo, Z. Chai, X. Rong, F. Shi, X.-J. Liu, Y. Wang, and J. Du, Quantum simulation for three-dimensional chiral topological insulator, *Phys. Rev. Lett.* **125**, 020504 (2020).
- [88] J. Niu, T. Yan, Y. Zhou, Z. Tao, X. Li, W. Liu, L. Zhang, H. Jia, S. Liu, Z. Yan, Y. Chen, and D. Yu, Simulation of higher-order topological phases and related topological phase transitions in a superconducting qubit, *Sci. Bull.* **66**, 1168 (2021).
- [89] B. Chen, S. Li, X. Hou, F. Ge, F. Zhou, P. Qian, F. Mei, S. Jia, N. Xu, and H. Shen, Digital quantum simulation of floquet topological phases with a solid-state quantum simulator, *Photonics Res.* **9**, 81 (2021).
- [90] D. Yu, B. Peng, X. Chen, X.-J. Liu, and L. Yuan, Topological holographic quench dynamics in a synthetic frequency dimension, *Light Sci. Appl.* **10**, 1 (2021).
- [91] J.-H. Zhang, B.-B. Wang, F. Mei, J. Ma, L. Xiao, and S. Jia, Topological optical raman superlattices, *Phys. Rev. A* **105**, 033310 (2022).
- [92] S. R. Manmana, S. Wessel, R. M. Noack, and A. Muramatsu, Strongly correlated fermions after a quantum quench, *Phys. Rev. Lett.* **98**, 210405 (2007).
- [93] A. Polkovnikov, K. Sengupta, A. Silva, and M. Vengalattore, Colloquium: Nonequilibrium dynamics of closed interacting quantum systems, *Rev. Mod. Phys.* **83**, 863 (2011).
- [94] T. Kiendl and F. Marquardt, Many-particle dephasing after a quench, *Phys. Rev. Lett.* **118**, 130601 (2017).
- [95] L. Zhang, L. Zhang, Y. Hu, S. Niu, and X.-J. Liu, Nonequilibrium characterization of equilibrium correlated quantum phases, *Phys. Rev. B* **103**, 224308 (2021).
- [96] M. Moeckel and S. Kehrein, Interaction quench in the Hubbard model, *Phys. Rev. Lett.* **100**, 175702 (2008).
- [97] L. Han and C. A. R. Sá de Melo, Evolution from BCS to BEC superfluidity in the presence of spin-orbit coupling, *Phys. Rev. A* **85**, 011606(R) (2012).
- [98] M. S. Foster, M. Dzero, V. Gurarie, and E. A. Yuzbashyan, Quantum quench in a $p + ip$ superfluid: Winding numbers and topological states far from equilibrium, *Phys. Rev. B* **88**, 104511 (2013).
- [99] Y. Dong, L. Dong, M. Gong, and H. Pu, Dynamical phases in quenched spin-orbit-coupled degenerate fermi gas, *Nat. Commun.* **6**, 1 (2015).
- [100] I. V. Gornyi, A. D. Mirlin, and D. G. Polyakov, Interacting electrons in disordered wires: Anderson localization and low-T transport, *Phys. Rev. Lett.* **95**, 206603 (2005).
- [101] J. Eisert, M. Friesdorf, and C. Gogolin, Quantum many-body systems out of equilibrium, *Nat. Phys.* **11**, 124 (2015).
- [102] N. Y. Yao, A. C. Potter, I.-D. Potirniche, and A. Vishwanath, Discrete time crystals: Rigidity, criticality, and realizations, *Phys. Rev. Lett.* **118**, 030401 (2017).
- [103] S. Peotta, F. Brange, A. Deger, T. Ojanen, and

- C. Flindt, Determination of dynamical quantum phase transitions in strongly correlated many-body systems using loschmidt cumulants, *Phys. Rev. X* **11**, 041018 (2021).
- [104] W. Jia, Z.-H. Huang, X. Wei, Q. Zhao, and X.-J. Liu, Topological superfluids for spin-orbit coupled ultracold Fermi gases, *Phys. Rev. B* **99**, 094520 (2019).
- [105] P. D. Powell, G. Baym, and C. A. R. Sá de Melo, Superfluid transition temperature and fluctuation theory of spin-orbit-and Rabi-coupled fermions with tunable interactions, *Phys. Rev. A* **105**, 063304 (2022).
- [106] T. Esslinger, Fermi-Hubbard physics with atoms in an optical lattice, *Annu. Rev. Condens. Matter Phys.* **1**, 129 (2010).
- [107] L. Tarruell and L. Sanchez-Palencia, Quantum simulation of the Hubbard model with ultracold fermions in optical lattices, *C. R. Phys.* **19**, 365 (2018).
- [108] L. Ziegler, E. Tirrito, M. Lewenstein, S. Hands, and A. Bermudez, Correlated Chern insulators in two-dimensional Raman lattices: a cold-atom regularization of strongly-coupled four-Fermi field theories, [arXiv:2011.08744](https://arxiv.org/abs/2011.08744).
- [109] L. Ziegler, E. Tirrito, M. Lewenstein, S. Hands, and A. Bermudez, Large-N Chern insulators: Lattice field theory and quantum simulation approaches to correlation effects in the quantum anomalous Hall effect, *Ann. Phys.* **439**, 168763 (2022).
- [110] E. Tirrito, S. Hands, and A. Bermudez, Large-S and tensor-network methods for strongly-interacting topological insulators, *Symmetry* **14**, 799 (2022).
- [111] H. Guo and S.-Q. Shen, Topological phase in a one-dimensional interacting fermion system, *Phys. Rev. B* **84**, 195107 (2011).
- [112] B. Song, C. He, S. Niu, L. Zhang, Z. Ren, X.-J. Liu, and G.-B. Jo, Observation of nodal-line semimetal with ultracold fermions in an optical lattice, *Nat. Phys.* **15**, 911 (2019).
- [113] Y.-J. Lin, K. Jiménez-García, and I. B. Spielman, Spin-orbit-coupled Bose-Einstein condensates, *Nature* **471**, 83 (2011).
- [114] P. Wang, Z.-Q. Yu, Z. Fu, J. Miao, L. Huang, S. Chai, H. Zhai, and J. Zhang, Spin-orbit coupled degenerate Fermi gases, *Phys. Rev. Lett.* **109**, 095301 (2012).
- [115] R. A. Williams, M. C. Beeler, L. J. LeBlanc, K. Jiménez-García, and I. B. Spielman, Raman-induced interactions in a single-component Fermi gas near an *s*-wave Feshbach resonance, *Phys. Rev. Lett.* **111**, 095301 (2013).
- [116] T. L. Gilbert, A phenomenological theory of damping in ferromagnetic materials, *IEEE Trans. Magn.* **40**, 3443 (2004).